

HEATING IN THE ACCRETED NEUTRON STAR OCEAN: IMPLICATIONS FOR SUPERBURST IGNITION

SANJIB GUPTA¹, EDWARD F. BROWN, HENDRIK SCHATZ, PETER MÖLLER¹, KARL-LUDWIG KRATZ^{2,3}

Department of Physics & Astronomy, National Superconducting Cyclotron Laboratory, and the Joint Institute for Nuclear Astrophysics, Michigan State University, East Lansing, MI 48824

submitted to *The Astrophysical Journal*

ABSTRACT

We perform a self-consistent calculation of the thermal structure in the crust of a superbursting neutron star. In particular, we follow the nucleosynthetic evolution of an accreted element from deposition into the atmosphere down to neutron drip density. We include temperature-dependent continuum electron capture rates and realistic sources of heat loss by thermal neutrino emission from the crust and core. We show that, in contrast to previous calculations, electron captures to excited states and subsequent γ -emission significantly reduces the local heat loss due to weak-interaction neutrinos. Furthermore, temperature-sensitive (γ, n) rates trigger further energy deposition as the distribution of nuclei evolves toward a lower neutron separation energy. Depending on the initial composition these reactions release up to a factor of ten times more heat at densities $< 10^{11} \text{ g cm}^{-3}$ than obtained previously. This heating reduces the ignition depth of superbursts. In particular, it reduces the discrepancy noted by Cumming et al. between the temperatures needed for unstable ^{12}C ignition on timescales consistent with observations and the reduction in crust temperature from Cooper pair neutrino emission.

Subject headings: dense matter — nuclear reactions, nucleosynthesis, abundances — stars: neutron—X-rays: binaries — X-rays: bursts

1. INTRODUCTION

The ability to regularly monitor the X-ray sky with instruments such as *RXTE* and *BeppoSAX* has produced many exciting discoveries in the last few years. An excellent example are superbursts (for a review see Kuulkers 2003). Like normal type I X-ray bursts (for a review, see Strohmayer & Bildsten 2004), superbursts are characterized by a rapid rise in the lightcurve followed by a quasi-exponential decay; when compared to type I X-ray bursts, superbursts are roughly $\sim 10^3$ times more energetic, have cooling timescales of hours, and recur on timescales of years. For one source, 4U 1636–53, three superbursts have been observed over a span of 4.7 yr (Wijnands 2001; Kuulkers et al. 2004). Although most superbursts are observed at mass accretion rates $0.1\text{--}0.3 \dot{M}_{\text{Edd}}$, with $\dot{M}_{\text{Edd}} \approx 10^{18} \text{ g s}^{-1}$ being the Eddington accretion rate, recently in t Zand, Cornelisse, & Cumming (2004a) detected superbursts from the rapidly accreting source GX 17+2.

The currently favored scenario for these superbursts is the thermally unstable ignition of ^{12}C at densities $\sim 10^8\text{--}10^9 \text{ g cm}^{-3}$ (Cumming & Bildsten 2001; Strohmayer & Brown 2002). Cumming & Macbeth (2004) demonstrated that the superburst lightcurve after the peak luminosity has been reached declines as a broken power law, with the early behavior dependent on the burst energy and the later behavior dependent on the ignition depth. This behavior has been observed (Cumming et al. 2006). The ability to constrain the burst energetics and ignition depth is crucial, not only for understanding the ignition of ^{12}C in a heavy-element bath, but also for probing the interior of the neutron star (Brown 2004; Cooper & Narayan 2005; Cumming et al. 2006). Brown (2004) demonstrated that the temperature at densities $\sim 10^9 \text{ g cm}^{-3}$ is sensitive to the ther-

mal conductivity of the inner crust and the neutrino emissivity of the core; this was confirmed by Cooper & Narayan (2005) in a more extensive study. Recently, Cumming et al. (2006) showed that the neutrino emission from Cooper pairing of singlet neutrons in the inner crust limited the temperature at neutron drip to be $\lesssim 5 \times 10^8 \text{ K}$. Taken at face value, this would lead to superburst ignition depths about an order of magnitude deeper than the $0.5\text{--}3 \times 10^{12} \text{ g cm}^{-2}$ deduced from observations, and correspondingly to recurrence times that are about an order of magnitude longer than observed. This led Page & Cumming (2005) to speculate that the superbursters might in fact be strange stars.

The unstable ignition of ^{12}C depends critically on the thermal structure of the outer crust and is sensitive to the heat sources located there. The outer crust of the neutron star is composed of nuclei and degenerate electrons and exists where the electron chemical potential $\mu_e \lesssim 30 \text{ MeV}$ (see Pethick & Ravenhall 1998, for a lucid discussion). The ashes of hydrogen, helium, and carbon burning in the neutron star envelope are continuously compressed by the ongoing accretion of matter and incorporated into the crust. The increasing density induces nuclear reactions at various depths that can release energy. *We show that most of this energy is deposited in the crust, rather than being carried away by neutrinos. This leads to a hotter crust and decreases superburst ignition depths and recurrence times.*

Previous studies of the crust heat sources (Sato 1979; Haensel & Zdunik 1990, 2003) used a single representative isotope (^{56}Fe and ^{106}Pd , respectively) for the product of H/He burning. Haensel & Zdunik (1990) found that electron captures would occur in two stages (see Fig. 1). The first electron capture (labeled ① in Fig. 1) would occur when $\mu_e \approx E_{\text{thr}}^{(Z,A)}$ for capture onto an even-even nucleus: $(Z, A) + e^- \rightarrow (Z-1, A) + \nu_e$, where Z and A are even. Here the threshold is $E_{\text{thr}} = E_{\text{thr,gs-gs}} + E_{\text{exc}}$, where the threshold for the ground-state-to-ground-state transition $E_{\text{thr,gs-gs}}$ is computed from atomic mass differences and therefore includes the elec-

Electronic address: guptasanjib@lanl.gov, ebrown@pa.msu.edu, schatz@nsl.msu.edu, moeller@lanl.gov, kkratz@uni-mainz.de

¹ Theoretical Division, Los Alamos National Laboratory, NM 87545

² Max-Planck-Institut für Chemie, Otto-Hahn-Institut, Joh.-J.-Becherweg 27, D-55128 Mainz, Germany

³ HGF VISTARS, D-55128 Mainz, Germany

tron rest mass, and where E_{exc} is the energy of the lowest excited state into which the capture can proceed. Because of the odd-even staggering of the nuclear masses, $E_{\text{thr,gs-gs}}^{(Z-1,A)}$ for electron capture onto the resulting odd-odd nucleus $(Z-1,A)$ is less than $E_{\text{thr,gs-gs}}^{(Z,A)}$. Consequently, $\mu_e > E_{\text{thr,gs-gs}}^{(Z-1,A)}$ and a second electron capture $(Z-1,A) + e^- \rightarrow (Z-2,A) + \bar{\nu}_e$ immediately follows. Where experimental data were lacking, which is the case for the vast majority of nuclei, the heat deposited into the crust Q was calculated assuming that the capture was into the ground state of the daughter nucleus (Fig. 1, ④). The heat deposited into the crust is then estimated as (Haensel & Zdunik 2003) $Q = (\mu_e - E_{\text{thr,gs-gs}})/4$, where the factor 1/4 arises from the integral over the reaction phase space in the limit that $(\mu_e - E_{\text{thr}})/\mu_e \ll 1$. This estimate assumes that final states are very low in excitation energy so that the contribution to the heat deposition from the radiative de-excitation of the daughter nucleus is always negligible compared to the heat release from the electron capture. In this picture, 75% of the nuclear energy release is emitted in form of neutrinos.

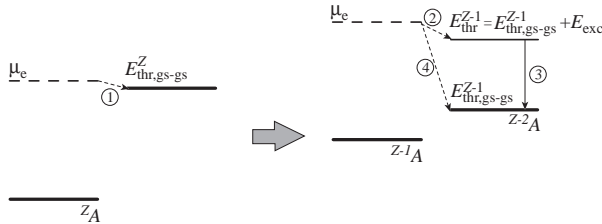


FIG. 1.— Illustration of an electron capture for which the first transition ① proceeds to the ground state of nucleus $Z-1A$, but the second transition instead goes to an excited state ② followed by a radiative de-excitation ③. Previous works assumed that the second transition always went to the ground state ④.

In this paper, we calculate heating from nuclear reactions in the outer crust (where the mass density is less than neutron drip, $\sim 10^{11} \text{ g cm}^{-3}$) using realistic electron capture rates obtained by microscopic calculations of the transition matrix elements between the parent ground state and daughter excited states multiplied with the phase space factor corresponding to the Q -value of the decay. The rates depend on the excitation energy and the ambient temperature and density. We use a full reaction network having temperature- and density- dependences and we include not only electron captures but also neutron photodisintegration (γ, n) and neutron capture (n, γ) reactions. Instead of starting with a single nucleus, we follow the actual mix of nuclei initially produced by surface burning, both from the rp-process (§ 2.2.1) and an NSE mixture formed during a superburst (§ 2.2.2). We find that electron captures deposit considerably more energy in the crust than in previous estimates (Haensel & Zdunik 2003). This larger heat deposition is mainly due to the electron captures populating excited states with energy E_{exc} (Fig. 1, ②), rather than capturing into the ground state as assumed previously. The populated excited states then radiatively de-excite (Fig. 1, ③), depositing the entire excitation energy as heat into the crust. We also introduce an approximate model that gives a good estimate of the heating in the outer regions of the crust for an arbitrary mixture in § 2.3 and describe the implications for superburst ignition in § 3.2.

2. REACTIONS IN THE OUTER CRUST

The evolution of the composition and the associated nuclear energy generation is calculated with a nuclear reaction network of ≈ 1500 isotopes covering the mass range $A = 1-106$ and extending from proton-rich rp-process ashes to the neutron dripline. In this section, we first describe how the electron capture and β -decay rates are calculated. We next describe the heating in the outer crust with two different initial compositions: rp-process and superburst ashes. Building on these results, we then develop a method to approximate the heating in the outer crust for an arbitrary composition.

2.1. The Nuclear Model

We calculate electron capture rates for each time step of the integration of the reaction network using a table of electron capture transition strengths as a function of excitation energy in the daughter nucleus and a fast analytic phase space approximation (Becerril Reyes et al. 2006) that is valid for low temperatures. This phase space calculation takes into account the temperature and density dependence of the electron capture rates and is accurate enough to handle the sharp reaction thresholds, which make table interpolation impossible. Temperatures and densities are calculated self-consistently from the energy generation and composition determined by the reaction network using an iterative procedure with the thermal model discussed in section 3.

Our nuclear model used to calculate the transition strength functions is described in detail in Möller & Randrup (1990) and here we just give a summary of its properties. We consider only allowed Gamow-Teller transition strength, which is computed in the quasi-particle random-phase approximation (QRPA). To obtain the wave functions we solve the Schrodinger equation for a deformed folded-Yukawa single-particle potential. We then add pairing and Gamow-Teller residual interactions treated in the Lipkin-Nogami and random phase approximations. Ground-state deformation parameters and masses are obtained from the finite-range droplet model (Möller et al. 1995). We calculate neutrino losses for each transition, rather than assuming that a fixed fraction of $(\mu_e - E_{\text{thr}})$ is lost to neutrinos. As temperatures are low and radiative de-excitation timescales are much faster than weak interaction timescales, we assume that the parent nuclei are in their ground states.

For the depths considered in this calculation, electron-capture-induced neutron emission is not important. We further assume that β^- decay is always completely blocked. This is a good assumption in most cases as temperatures are low, and because most electron captures either proceed in a double step, with the second step proceeding with $\mu_e \gg E_{\text{thr,gs-gs}}$, or, if they occur at threshold, populate excited states in the final nucleus. In both cases, μ_e is much larger than the β^- decay Q -value, which is always equal or less than the ground state to ground state electron capture threshold. We will discuss some possible exceptions to this in § 4.

While our main goal is to explore the crust heating within the framework of electron capture rates computed from the QRPA strength functions, we did adjust the transition energies in one case, for which the QRPA predictions are at odds with experimental information, and for which this has a strong effect on the crustal heating. Our model predicts that the electron capture on ^{104}Rh proceeds to an excited state at 5.3 MeV, which would result in strong heating at that depth. Experimental data (Frevert, Schoneberg, & Flammersfeld 1965) shows, however, that while ^{104}Rh is β^- unstable, it also has a small ground-state-to-ground-state electron capture branch

with a positive Q -value. As a result there is no nuclear excitation energy released and the heat deposition from this reaction is much smaller than predicted from our model.

In addition to the weak interaction rates, our network includes neutron capture rates, calculated with the statistical Hauser-Feshbach model NON-SMOKER (Rauscher & Thielemann 2000). The corresponding (γ, n) rates are calculated from detailed balance. For the conditions considered here the neutrons are always non-degenerate; denoting the degeneracy by $\eta = \mu_n (k_B T)^{-1}$, we require for degeneracy an abundance

$$Y_n > 0.015 \left(\eta T_9^{3/2} \right)^{3/2} \rho_{12}^{-1}. \quad (1)$$

For typical values $T_9 = 0.5$, $\rho_{12} = 0.2$, and taking $\eta = 0.1$ as a fiducial threshold, we have $Y_n > 8.4 \times 10^{-4}$ as the abundance threshold beyond which neutron degeneracy becomes important. We are well below this throughout our computational domain. We also do not account for the effect of a large electron plasma temperature; at the largest densities we consider, the plasma temperature is only of the order of the neutron separation energy and its effect on (γ, n) reaction rates should therefore be negligible. For consistency we use the NON-SMOKER rates based on masses predicted by the finite-range droplet model.

The output of the reaction network is the crust composition and heat deposition $dQ = dE_{\text{nuc}} + dE_e - dE_\nu$ for each timestep $dt = (\rho/\dot{m}) dr$. Here $dE = \sum_i dY_i BE_i$ is the nuclear energy generation calculated from the abundance change dY_i and binding energy BE_i of each isotope i , $dE_e = \mu_e dY_e$ is the energy change due to changes in electron abundance, and dE_ν is the energy released as neutrinos from electron capture. Thermal neutrino losses, i.e., neutrino-pair bremsstrahlung and Cooper-pair neutrino emission, are included as cooling terms ε_ν in the thermal calculation (cf. § 3.1). We neglect the contribution from the change in Coulomb lattice energy dE_{lat} arising from the change in nuclear charge during an electron capture. Consider a single ion species (Z, A) with number density n_{ion} . The lattice energy is mostly due to the Madelung term, $E_{\text{lat}} \approx -0.9(n_{\text{ion}}/\rho)k_B T \Gamma$, where $\Gamma = (Ze)^2/(ak_B T)$ and a is the mean ion spacing. The ratio of the lattice energy to electron energy is therefore $\propto \alpha Z^2/3$, where $\alpha = e^2/\hbar c$; with the numerical coefficients inserted this ratio is $\approx 3 \times 10^{-3} Z^2/3 \ll 1$ throughout the outer crust. As a result, the shift in the location of the transitions is small. Moreover, for a two-step electron capture, the contribution to dQ comes from the difference in dE_{lat} between the two transitions, i.e., in the relative shift of the two transitions. This difference contributes $\approx 76 \text{ keV u}^{-1} (\rho/10^{10} \text{ g cm}^{-3})^{1/3} A^{-4/3} \lesssim 1 \text{ keV u}^{-1}$ for the cases we consider here.

2.2. Heat Sources in the Outer Crust

Using the model described above, we computed the heat release for different starting compositions. In the following discussions, we highlight the dominant transitions in each.

2.2.1. Rp-Process Ashes

We first calculate the heat sources in the outer crust using rp-process ashes from a one-zone X-ray burst model (Schatz et al. 2001). The peak of the nuclide distribution is around $A = 104$, and it is useful to compare our results with those of Haensel & Zdunik (2003), who started with a single nuclide, ^{106}Pd . The initial composition is dominated by ^{104}Cd

(mass fraction 25% by mass), ^{105}Cd (9.6% by mass), and ^{68}Ge (7.1% by mass). Other mass chains with mass fractions above 2% are $A = 64, 72, 76, 98, 103$, and 106. There are also some small residual amounts of ^{12}C (0.7% by mass) and ^4He (0.5% by mass). Once the fluid element has reached $\mu_e \approx 4 \text{ MeV}$ both ^4He and ^{12}C have fused into heavier elements via the 3α and the $^{12}\text{C} + ^{12}\text{C}$ reactions. Their abundances are so small, however, that they contribute a negligible amount of heating at these shallow depths.

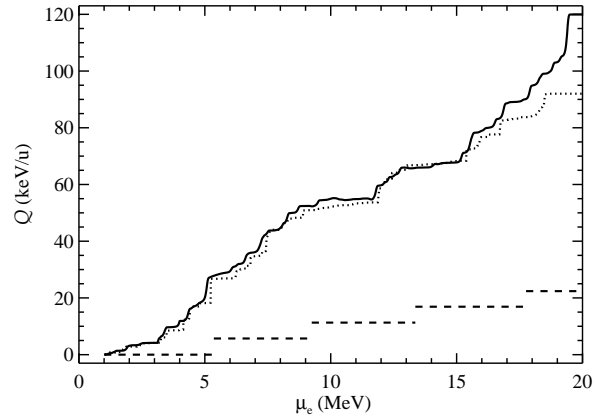


FIG. 2.— Integrated heat release in the crust from the compression of the rp-process ashes from X-ray bursts (solid line). For comparison, we also show (dashed line) the integrated heat released in the model of Haensel & Zdunik (2003), as well as the results from our approximate model (dotted lines, see § 2.3).

We start our calculation at $\mu_e \approx 0.38 \text{ MeV}$ ($\rho = 6.2 \times 10^6 \text{ g cm}^{-3}$). There is an initial spike in heating as the fluid element comes into β -equilibrium. This heating is an artifact of our calculation, but, being located at the outer boundary where T is fixed, does not affect the resulting thermal profile. As the fluid element is moved to greater depth, the rising μ_e induces electron captures that reduce $\langle Z \rangle$ while preserving $\langle A \rangle$. For $\mu_e \gtrsim 14 \text{ MeV}$ ($\rho \gtrsim 6 \times 10^{10} \text{ g cm}^{-3}$), $\langle A \rangle$ is no longer constant, as (γ, n) and (n, γ) reactions become important and alter the relative abundance of different mass chains. Fig. 2 shows the integrated deposited energy (solid line) as a function of μ_e . In this plot we set the integrated heat release to zero at $\mu_e = 1.0 \text{ MeV}$ so that we can compare our results to those of Haensel & Zdunik (2003, dashed line). In the range $1 \text{ MeV} < \mu_e < 14 \text{ MeV}$, electron captures deposit 66.3 keV u^{-1} , which considerably exceeds the previous estimate of 16.9 keV u^{-1} (Haensel & Zdunik 2003). In this range of μ_e , neutrinos carry away 37.2 keV u^{-1} .

This much larger heat deposition is due to our use of realistic electron capture rates, which often lead to the population of excited states in the daughter nucleus rather than the daughter ground state as assumed previously. Electron capture thresholds are therefore increased by these excitation energies. More importantly, however, the radiative de-excitation of the excited state deposits the excitation energy as heat, rather than having it carried off by neutrinos. Note that the sum of the heat deposited in the crust and the neutrino loss is 83.3 keV u^{-1} , which is only slightly larger than the comparable total for the calculation of Haensel & Zdunik (2003), where a single mass $A = 106$ was used.

Therefore, electron captures on even-even, odd-even, or even-odd nuclei, which tend to occur where the $\mu_e = E_{\text{thr}}$, can now deposit considerable amounts of heat. These reactions

were not considered as heat sources before, as it was assumed that they proceeded from ground state to ground state. In addition, for the electron captures on the odd-odd nuclei—the main heat sources in previous work—the fraction of energy lost to neutrinos is considerably reduced.

As an example, a prominent heat source that can be identified in Fig. 2 is the two step electron capture transition of ^{104}Ru into ^{104}Mo at around $\mu_e = 5.2$ MeV. The electron capture on ^{104}Ru has a threshold for the transition into the daughter ground state of $E_{\text{thr,gs-gs}} = 5.09$ MeV and is predicted to proceed to a low-lying state in ^{104}Tc at $E_{\text{exc}} = 0.15$ MeV. Therefore, this transition occurs at $\mu_e \approx E_{\text{thr,gs-gs}} + E_{\text{exc}} = 5.24$ MeV. The subsequent electron capture on ^{104}Tc has a lower ground state to ground state threshold $E_{\text{thr,gs-gs}} = 1.96$ MeV and is dominated by a transition to an excitation energy of $E_{\text{exc}} = 2.80$ MeV in ^{104}Mo . For the latter transition, about 75% of the transition energy $\mu_e - E_{\text{thr,gs-gs}} - E_{\text{exc}} = 0.48$ MeV is lost to neutrinos, but the entire excitation energy E_{exc} for both steps is deposited as heat, resulting in a total heat deposition of $Q = 3.07$ MeV per transition. The heat generated per accreted nucleon is then $Q \times Y_{104} = 8.6$ keV u^{-1} , with $Y_{104} = 2.8 \times 10^{-3}$ being the abundance in the $A = 104$ chain. If the electron capture on ^{104}Tc proceeded through the ground state of ^{104}Mo , as assumed in previous works, then about 75% of the entire transition energy $\mu_e - E_{\text{thr,gs-gs}} = 3.28$ MeV would be lost to neutrinos and the heat deposition would be reduced by a factor of 3.6 to about 0.82 MeV per transition. Another prominent heat source in the region $\mu_e \lesssim 14$ MeV is the two-step electron capture on ^{68}Fe at $\mu_e \approx 11.8$ MeV (with heat deposition $Q \times Y_{68} = 5$ keV u^{-1}).

Typically, transitions in even A chains, such as the electron capture on ^{104}Ru discussed above, occur as double steps due to the odd-even staggering of the electron capture thresholds, though exceptions can occur if the transitions populate high lying excited states. In contrast, thresholds in odd A chains tend to increase steadily with electron captures proceeding in single steps. However, there are also some important two-step electron captures in odd mass chains, most importantly the transition from ^{105}Rh into ^{105}Tc at $\mu_e = 4.4$ MeV. While the electron capture on ^{105}Rh has a ground-state-to-ground-state threshold of 1.6 MeV, the transition is predicted to mainly go to a 2.9 MeV excited state in ^{105}Ru . This effectively raises the threshold to ≈ 4.5 MeV. Therefore, even though the electron capture on ^{105}Rh occurs at an μ_e near this “effective” threshold, the full 2.9 MeV excitation energy is deposited into the crust. Following the electron capture onto ^{105}Rh , μ_e is then sufficient to overcome the 3.6 MeV threshold (which includes a final state excitation energy of 0.15 MeV) for electron capture $^{105}\text{Ru} \rightarrow ^{105}\text{Tc}$. In total this sequence deposits 3.8 keV u^{-1} into the crust ($Y_{105} = 1.3 \times 10^{-3}$).

The mass chains $A = 72, 76, 98,$ and 103 also contribute 2–3 keV u^{-1} each in the region $\mu_e < 14$ MeV. In total, there are about 15 transitions that generate 2 keV u^{-1} or more and that are responsible for about 66% of the total deposited heat. The remainder of the heating is produced by a larger number of less energetic electron captures.

A second source of heating that has not been considered at all in previous work is the capture of neutrons released by (γ, n) photodisintegration. Such reactions begin to occur at $\mu_e \gtrsim 14$ MeV. At this point electron captures on ^{103}Rb set in. However, the ^{103}Kr daughter has a neutron separation energy of just 1.9 MeV. Even though electron capture populates the

neutron bound ground state, ^{103}Kr is immediately destroyed by a (γ, n) reaction. A similar neutron source is $^{101}\text{Kr}(\gamma, n)$. ^{101}Kr has a neutron separation energy of 2.1 MeV and is populated by two successive electron captures starting on ^{101}Sr . Because our crust composition is a mix of a number of different nuclei with different mass numbers, the neutrons released by nuclei with low neutron separation energy tend to be recaptured quickly by nuclei with larger neutron capture Q -values. Only at greater depth where most A -chains have reached low neutron separation energies does an appreciable neutron abundance begin to appear. In the case considered here, the main capture reactions are $^{105}\text{Sr}(n, \gamma)^{106}\text{Sr}$ (Q -value 4.8 MeV) and $^{94}\text{Br}(n, \gamma)^{95}\text{Br}$ (Q -value 4.8 MeV), though there are many weaker reactions occurring. The produced nuclei are stable against electron capture and β^- decay at the depth where they are formed. In this particular case, therefore, neutron captures do not trigger additional weak reactions, but the difference between the neutron capture Q -value and the neutron separation energy of the neutron source (here about 2.8 MeV per reaction) still represents a significant contribution to the total heating.

An effect that we have not included in our calculations explicitly and that could in principle lead to additional cooling is an Urca process that might occur for single-step, ground-state-to-ground-state electron captures, when the subsequent electron capture is blocked until significantly higher density. If the temperature is sufficiently high for such an electron capture to occur pre-threshold, the reverse β^- decay is not blocked. Until μ_e has risen to a sufficiently large value the electron capture occurs in tandem with a ground-state-to-ground-state β^- decay in the reverse direction and an Urca process will result. While such transitions are rare (most electron captures proceed as double steps, or to excited states) there are a few cases where they do occur, particularly in odd-mass chains far from neutron sub-shell closures.

An example is ^{103}Y , which has a ground-state threshold $E_{\text{thr,gs-gs}} = 10.83$ MeV, while the electron capture daughter ^{103}Sr has $E_{\text{thr,gs-gs}} = 13.39$ MeV. For non zero temperature an Urca process can occur for a small range of μ_e where both, ^{103}Y electron capture and ^{103}Sr β^- decay are fast compared to the accretion timescale. Using the electron capture and β^- decay rates from our QRPA model we estimate that only a few Urca cycles can occur for the peak temperature and accretion rate considered here. With each cycle releasing about 0.135 MeV per nucleus, we find for this particular case an additional neutrino energy loss of 0.3 keV u^{-1} (using the abundance in the mass 103 chain $Y_{103} \sim 7 \times 10^{-4}$). Even if such processes occur for about a handful of transitions, the total neutrino energy loss from this effect will be negligible.

The rate of energy loss from neutrinos is obviously very sensitive to temperature; taking a logarithmic derivative of the rate for the pre-threshold capture suggests that the neutrino loss rate is $\propto T^7$. For the specific case considered here, the rate is so small that the contribution from this process is negligible for $T \lesssim 8 \times 10^8$ K. It would be interesting to explore this process in more detail with accurate electron capture and β^- rates for a range of temperatures and accretion rates.

2.2.2. Superburst ashes

The previous calculation described the evolution of ^{12}C -poor ashes produced during an rp-process in an X-ray burst. For accreting neutron stars that exhibit superbursts, which typically ignite at a density $\lesssim 10^9$ g cm^{-3} (Cumming et al.

2006), the burning during the superburst sets the initial crust composition rather than the X-ray burst. The composition in the region between the H/He burning shell and the carbon burning shell is also not well-described by X-ray burst ashes, as they do not contain sufficient amounts of ^{12}C to ignite superbursts. A better estimate for the initial composition in superburst systems might therefore be the ashes of *stable* hydrogen and helium burning, which do contain sufficient amounts of carbon at the accretion rates considered here (Schatz et al. 2003). We therefore perform a second calculation, in which we use as an initial composition the ashes of steady-state hydrogen and helium burning at the accretion rate of $0.3 \dot{M}_{\text{Edd}}$ (Schatz et al. 2003). This ash consists mainly of ^{52}Cr (36% by mass), ^{12}C (8% by mass), $^{57}\text{Co}+^{57}\text{Fe}$ (8% by mass together), ^{58}Ni (6% by mass), and ^{60}Ni (5% by mass). We then assume a composition change at $\mu_e = 4.3 \text{ MeV}$ ($\rho = 1.7 \times 10^9 \text{ g cm}^{-3}$) to the superburst ashes of Schatz, Bildsten, & Cumming (2003). The superburst ash consists mainly of ^{66}Ni (35% by mass), ^{64}Ni (15% by mass), and ^{60}Fe (14% by mass).

The electron captures on steady-state rp-process ashes in the region $0.45 \text{ MeV} < \mu_e < 4.3 \text{ MeV}$ result in 24 keV u^{-1} of heating, while the superburst ashes deposit 32.5 keV u^{-1} in the range $4.3 \text{ MeV} < \mu_e < 14 \text{ MeV}$. This latter heat deposition is slightly greater than half that deposited by the X-ray burst ashes in the same range of μ_e . Neutron processes set in much later at $\mu_e = 18.5 \text{ MeV}$, prior to which the energy deposition is dominated by just two transitions, $^{66}\text{Ni} \rightarrow ^{66}\text{Fe}$ at $\mu_e = 9.2 \text{ MeV}$ and $^{66}\text{Fe} \rightarrow ^{66}\text{Cr}$ at $\mu_e = 15.1 \text{ MeV}$. In both these transitions the second electron capture step populates relative high lying excited states at 3.6 MeV and 2.9 MeV respectively, hence the relatively large heat release. The fact that fewer transitions contribute to the heating is not unexpected as the composition is more homogeneous than in the case of the rp-process ashes.

2.2.3. Dependence on composition

The different heating obtained for rp- and superburst ashes illustrates clearly the composition dependence of crustal heating, when taking into account electron captures into excited states. The excitation energies populated by allowed Gamow-Teller transitions depend strongly on nuclear structure, in particular on shell and sub-shell closures. Fig. 3 shows for each parent nucleus the main excitation energy of the electron capture daughter. Clearly there are huge differences with particularly high excitation energies occurring near the shell closures. If the initial composition is such that significant amounts of nuclei get processed through such a region, particularly large heat deposition will occur. Away from shell closures nuclear deformation tends to fragment Gamow-Teller strength and suitable transitions are more likely to occur at lower excitation energies.

The type of neutron-induced reaction sequences and their energy release also depend strongly on composition. For the calculation based on superburst ashes, neutron-induced reactions are responsible for the largest heat source (34 keV u^{-1}) at around $\mu_e = 18.5 \text{ MeV}$ (see Fig. 2). The $^{64}\text{Cr} \rightarrow ^{64}\text{Ti}$ electron capture transition does occur there and contributes somewhat. However, the energy deposition is greatly enhanced by neutron-induced reactions. Major initial neutron sources are (γ, n) reactions on ^{65}Cr and on ^{66}V , which have low neutron separation energies of 1.9 MeV and 2.4 MeV respectively. The latter is being formed by electron capture on ^{66}Cr . As

this is an even A chain, this electron capture would usually be followed immediately by a second electron capture onto ^{66}V . However, in this case the (γ, n) rate exceeds the electron capture rate for ^{66}V . Clearly, absolute rates for electron captures and photodisintegration do matter in such cases. The released neutrons are quickly captured by $^{51-53}\text{K}$, $^{54-55}\text{Ca}$, ^{60}Ti , and initially also on ^{66}Cr . The neutron capture Q -values vary widely from 2–5 MeV but in the end a more neutron bound nucleus is formed causing some net heat release. In contrast to the neutron reactions discussed in connection with the rp ashes, some neutron captures form electron capture unstable nuclei triggering additional energy release by electron capture. The most important cases are neutron captures on ^{54}Ca , and ^{60}Ti , which are particularly abundant. In both cases electron captures following the neutron capture reaction lead to weakly neutron bound nuclei, which then undergo an additional (γ, n) reaction leading to a nucleus that is stable against β^- decay and electron capture. The resulting reaction chains are $^{54}\text{Ca}(n, \gamma)^{55}\text{Ca} \rightarrow ^{55}\text{K} \rightarrow ^{55}\text{Ar}(\gamma, n)^{54}\text{Ar}$ and $^{60}\text{Ti}(n, \gamma)^{61}\text{Ti} \rightarrow ^{61}\text{Sc} \rightarrow ^{61}\text{Ca}(\gamma, n)^{60}\text{Ca}$. As for each captured neutron a neutron is released, the neutrons serve only as catalysts and the chains can efficiently convert ^{54}Ca into ^{54}Ar and ^{60}Ti into ^{60}Ca as soon as a sufficient neutron abundance is established to drive the neutron capture rates. Because of the very large mass densities of $\rho \approx 10^{11} \text{ g cm}^{-3}$ and very long timescales $\tau \approx 10^{10} \text{ s}$ only very small neutron abundances are required. For example, the $^{60}\text{Ti}(n, \gamma)$ reaction rate at a temperature of 0.5 GK is $N_A \langle \sigma v \rangle = 5 \times 10^3 \text{ cm}^3 \text{ s}^{-1} \text{ g}^{-1}$, so that a minimum neutron abundance of just $Y_n = (\tau \rho N_A \langle \sigma v \rangle)^{-1} = 10^{-25}$ is needed to trigger this reaction. Both electron captures and neutron reactions contribute to the energy release in these reaction chains. Nevertheless, the net effect of these reaction chains is to facilitate the conversions of ^{54}Ca into ^{54}Ar and of ^{60}Ti into ^{60}Ca via an alternative path so that they can occur already at a lower Fermi energy compared to the simple electron capture transformations. The energy release will therefore be lower than if these reactions would have occurred via direct electron captures at greater depth. However, as soon as neutrons are released a number of such reaction chains, together with other neutron related reactions, occur simultaneously leading to the large net heating at that depth.

Clearly neutron-induced reactions are important and are extremely composition sensitive. This is already illustrated by the very different reactions that occur in the case of rp-ashes and the superburst ashes. Not only is it important how much abundance is in the neutron releasing mass chains that reach low neutron separation energies first (usually only one nucleus exists in a mass chain at a particular depth and the heavier, odd-mass chains lose neutrons first), but it is also critical whether nuclei are available in other mass chains at the time the neutrons are released. Depending on the composition, there will be a depth where neutron emission continues to occur and no suitable neutron capture targets are around. From there on an appreciable neutron abundance will build up. Therefore, depending on the composition and the temperature, we expect that (γ, n) reactions tend to shift the onset of neutron drip to smaller depths than previously assumed.

2.3. An Approximate Model

To explore the composition dependence further, and to disentangle the impact of the various differences to previous models more clearly, we developed a simplified model of the

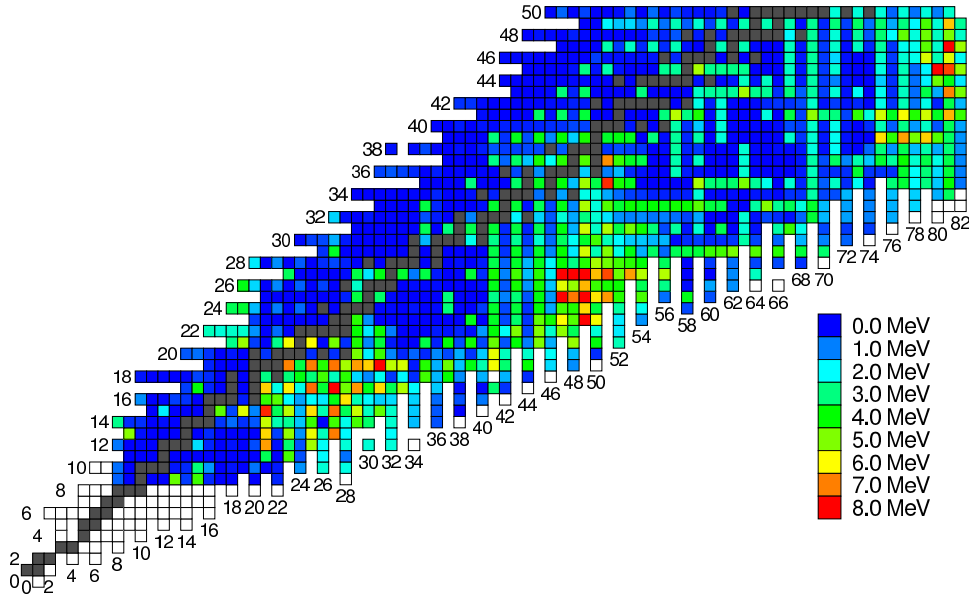


FIG. 3.— For each parent nucleus we show the excitation energy of the dominant state in the daughter nucleus populated by electron capture. Electron capture sequences passing through regions with high excitation energies in the daughter will result in increased heat deposition.

heating in the neutron star crust. In the spirit of some previous studies (Haensel & Zdunik 1990, 2003) we limit the model to electron captures only (no neutron reactions), we assume that electron captures proceed immediately when μ_e reaches or exceeds the threshold, and we assume that 75% of the electron capture transition energy is released in form of neutrinos. However, in contrast to previous work we do take into account that electron captures populate excited states in the daughter nuclei. We make the simplifying assumption that only the lowest lying daughter state with significant strength is populated.

To test this model we calculate the heat release as a function of depth for our initial rp-process ashes and compare the result (*dotted line*, Fig. 2) with the full network calculations for the rp-process burst ashes. Up to $\mu_e \approx 14$ MeV there is mostly good agreement. The slight offset at low μ_e is because the tabulation of the approximate model does not include captures at $\mu_e < 2.0$ MeV. The differences at higher μ_e show the influence of neutron induced reactions that are neglected in the analytic approach. For captures onto nuclei for which $\mu_e \gg E_{\text{thr}}$ our approximate model also underestimates the fraction of heat carried off by the neutrino. Nevertheless, this approximate model provides a first estimate of the crustal heating.

To explore the composition dependence further, Figure 4 maps out the heating, per nucleon, deposited in the crust as a function of mass number A at each depth μ_e , if the crust were composed of a single species with that mass number. For each A , we start with an initial isotope (Z, A) that is stable at the low-density boundary. We then use our analytical model to trace the heat deposition from successive electron captures with increasing μ_e . The area of each dot indicates the heat deposited in the crust for each transition, and its vertical location indicates the μ_e at the transition. The largest heat deposit is for $A = 38$ at $\mu_e = 17.3$ MeV with $Q = 0.28$ MeV u^{-1} . For this calculation we only include electron captures in the region $\mu_e < 20$ MeV.

In Fig. 4 we also show the total deposited heat as a func-

tion of the mass number A for each mass chain (*top panel, black histogram*). The greatest crustal heating would occur for a composition dominated by $A = 38$ or $A = 42$ with heat deposition reaching 0.45 MeV u^{-1} . Heavy ashes tend to release less energy per nucleon as excitation energies are similar but the nuclei include more nucleons. Nevertheless, shell effects lead to large heating for $A = 68$ – 91 with particularly high values for $A = 70, 84, 86,$ and 88 . In systems without superbursts, rp-process ashes rich in such nuclei would lead to a hotter crust. Superburst ashes in the mass range $A = 60$ – 66 and the rp-ashes dominated by $A = 104$ are less favorable for heating the crust.

For comparison, we also show the heat deposition calculated with the same method but assuming ground-state transitions only (*grey histogram*). Clearly taking into account realistic transition energies for electron captures leads to a dramatic increase in heat deposition that is strongly composition dependent.

3. THE THERMAL STRUCTURE OF THE CRUST

Having described our nuclear model for computing the electron capture rates and heating in the outer neutron star crust, we now turn to computing the thermal structure of the crust. As we shall describe, our thermal model is coupled to the reaction network, so that our solution is self-consistent. Our thermal model is the same as developed by Brown (2000, 2004) and we shall only summarize its essential properties here.

3.1. Computational Method

Over the crust, the gravitational potential $\Phi \approx \frac{1}{2}c^2 \ln(1 - 2GM/rc^2)$ is nearly constant; moreover, we are always in hydrostatic equilibrium and can approximate the pressure as being nearly independent of temperature. Under these approximations, we then solve the equations for temperature, luminosity, and nuclear heating,

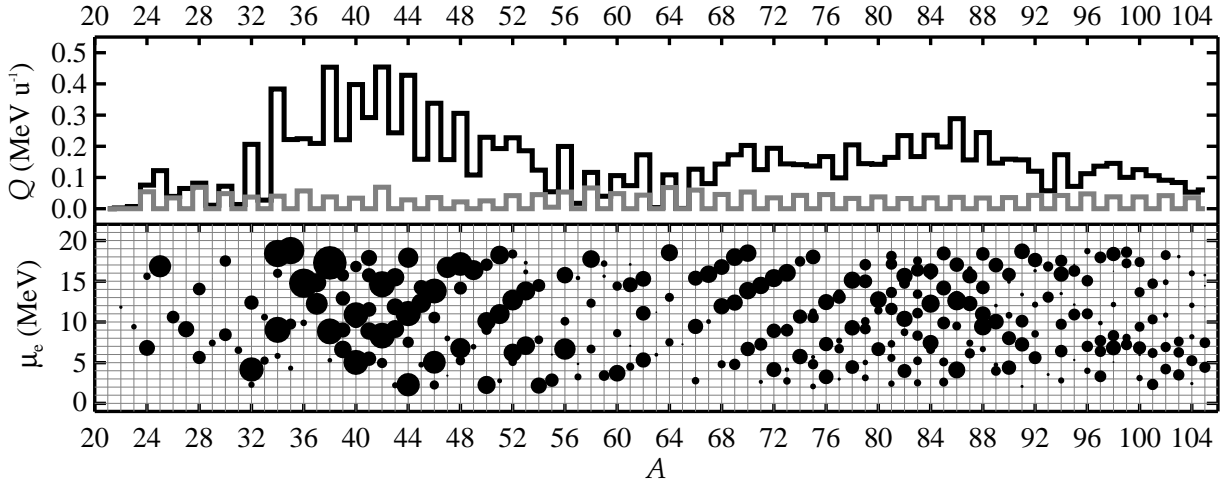


FIG. 4.— Electron captures in the outer crust. The mass number A is along the horizontal axis; accretion pushes the fluid to greater μ_e , which is upward on the bottom panel. Each dot on the bottom plot indicates the heat deposited into the crust by a given mass chain at that μ_e , with the area of each dot being proportional to the amount of heat deposited. The top panel shows the total heat deposited in the crust (*dark histogram*) for that mass chain, as described in 2.3. In particular, the heat released by (n, γ) reactions is neglected. For comparison, the heat that would be deposited if all transitions were ground-state-to-ground-state is also shown (*top panel, grey histogram*).

$$\frac{dT}{dr} = -\frac{L(1+z)}{4\pi r^2 K} \quad (2)$$

$$e^{-2\Phi/c^2} \frac{d(e^{2\Phi/c^2} L)}{dr} = \frac{dL_{\text{nuc}}}{dr} - 4\pi r^2 (1+z) \epsilon_\nu, \quad (3)$$

$$\frac{dL_{\text{nuc}}}{dr} = \dot{M} Q(r) u^{-1} \quad (4)$$

where $1+z = (1 - 2GM/rc^2)^{-1/2}$ is the gravitational redshift and $Q(r)$ is the heat deposited per accreted nucleon as computed from our reaction network. For our underlying neutron star model, we use for the core an analytical density prescription $\rho = \rho_0 [1 - (r/R)^2]$ (Tolman 1939), where $\rho_0 = 15(8\pi)^{-1} MR^{-3}$ with $R = (2GM/c^2) [1 - (1+z)^{-2}]^{-1/2}$. This prescription gives a reasonable approximation to the $\rho(r)$ that would be obtained from a modern nuclear EOS (see Lattimer & Prakash 2001, and references therein). With this choice for the EOS, the mass of the neutron star M and redshift z specify the mechanical structure of the star. We choose the crust-core boundary to be at a transition density $1.6 \times 10^{14} \text{ g cm}^{-3}$, which is the density found by a Maxwell construction using an EOS for the inner crust (Negele & Vautherin 1973) and the core EOS (Akmal, Pandharipande, & Ravenhall 1998). We then adopt a neutron star of mass $1.6 M_\odot$, and set the radius at the crust-core boundary to 10.5 km. This makes $[1 - 2GM/(rc^2)]^{-1/2} = 1.35$ at this point. Our neutron star then has a radius 10.8 km and a surface gravity $2.43 \times 10^{14} \text{ cm s}^{-2}$.

For our numerical calculations, we use an accretion rate, measured in the rest frame at the surface, of $\dot{M} = 3.0 \times 10^{17} \text{ g s}^{-1}$; the local accretion rate, per unit area, is then $2.1 \times 10^4 \text{ g s}^{-1} \text{ cm}^{-2}$ and the luminosity (for spherical accretion) is 0.3 of the Eddington luminosity for a solar composition. The core neutrino emissivity is modified Urca with an emissivity $10^{20} (T/10^9 \text{ K})^8 \text{ ergs cm}^{-3} \text{ s}^{-1}$. Note that because our starting density is $\rho = 6.2 \times 10^6 \text{ g cm}^{-3}$, which is just below where the rp-process burning has concluded, we

do not resolve the H/He burning shell in the envelope. Observations of the ratio of persistent fluence to burst fluence suggest that a good fraction of the accreted H/He burns stably (in't Zand et al. 2004b), so we set the temperature at this boundary to $4.2 \times 10^8 \text{ K}$, which is computed by integrating steady H burning (Schatz et al. 1999) at a local accretion rate of $\dot{m} = 2.6 \times 10^4 \text{ g s}^{-1} \text{ cm}^{-2}$.

Solving equations (2) and (3) requires the equation of state, thermal conductivity K and neutrino emissivity ϵ_ν . We use a tabulated electron equation of state (Timmes & Swesty 2000) with ion electrostatic interactions (Farouki & Hamaguchi 1993). The pressure of the free neutrons is computed using a zero-temperature compressible liquid-drop model (Mackie & Baym 1977). Heat is transported by degenerate, relativistic electrons—our treatment of the electron scattering frequency follows (Brown, Bildsten, & Chang 2002; Brown 2004) and we presume that the crust has a completely disordered (Jones 2004) lattice so that the heat transport is controlled by electron-impurity scattering (Itoh & Kohyama 1993).

Our neutrino emissivity in the crust, ϵ_ν includes contributions from bremsstrahlung (Pethick & Thorsson 1994) and Cooper pairing of 1S_0 neutrons (Yakovlev, Kaminker, & Levenfish 1999) in the inner crust. For the critical temperature T_c of the paired neutrons, we choose a Gaussian in neutron Fermi momentum k_F with a maximum $\max(k_B T_c) = 0.8 \text{ MeV}$ at $k_F = 0.8 \text{ fm}^{-1}$, and a width 0.28 fm^{-1} . These parameters are chosen to closely reproduce the $T_c(k_F)$ of Ainsworth, Wambach, & Pines (1989). As shown by Cumming et al. (2006), the strong temperature sensitivity of the neutrino emissivity ϵ_ν^C makes the crust temperature rather insensitive to the precise dependence of the critical temperature on density. Recently (Leinson & Perez 2006) argued that the adopted rate ϵ_ν^C was overestimated by a factor $(v_F/c)^4 \gg 1$, where v_F is the neutron Fermi velocity. We therefore performed additional calculations with ϵ_ν^C reduced by this factor.

We couple the steady-state thermal equations (2)–(4) with the reaction network calculations via an iterative proce-

Starting from an initial choice for the temperature profile $T(r)$, we integrate the reaction network along the path $\{T[t(r)], \rho[t(r)]\}$, where t refers to the Lagrangian time since the fluid element was deposited onto the star; in our plane-parallel approximation, $t(r) = y(r)/\dot{m}$, with $y \approx P/g$ being the column depth $\int \rho dr$. We stop our integration where the neutron abundance begins to rise steeply ($\rho \gtrsim 2 \times 10^{11} \text{ g cm}^{-3}$). The output of the reaction network gives us the local heat $Q(r)u^{-1}$ deposited in the shell $\{r, r + \Delta r\}$ per accreted nucleon. We use $Q(r)u^{-1}$ and the abundance vector $\vec{Y}(r)$ to solve equations (2)–(4) and construct a new thermal profile. For the inner crust we use the composition and heating from Haensel & Zdunik (2003)⁴. We then use the resulting thermal profile to update the network calculation, and we repeat this process until the thermal profile has converged. Typically only a few iterations are required, as the heating from electron captures is insensitive to the crust temperature.

As an example, we illustrate in Fig. 5 the results obtained when we start with the ashes of rp-process burning, which shows the temperature in units of 10^9 K (*top panel*). We also plot in Fig. 5 the luminosity L (*bottom panel*), which is multiplied by u/\dot{M} so that it is in units of MeV. We show two cases, one with the standard neutrino emissivity ϵ_ν^C (*dotted line*) and the other with ϵ_ν^C suppressed according to Leinson & Perez (2006, *solid lines*). Finally, for comparison, we show the thermal profiles obtained with the composition and heating of Haensel & Zdunik (2003, *top panel, grey lines*).

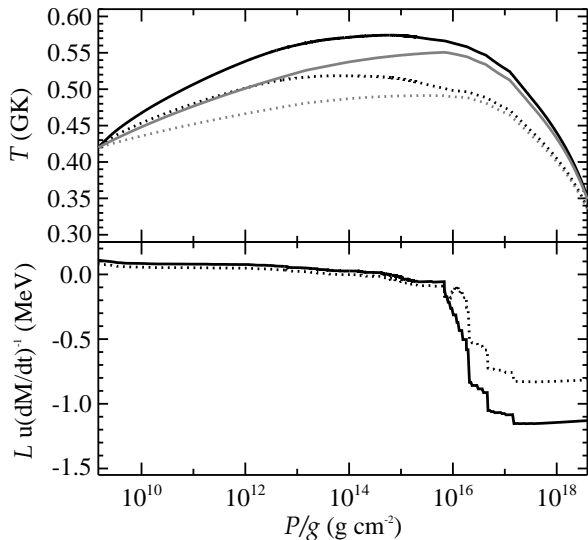


FIG. 5.— Temperature (*top*) and luminosity (*bottom*) in the neutron star crust, as functions of P/g , for a crust composed of heavy rp-process nuclei. We measure the luminosity in units of $\dot{M} \times \text{MeV } u^{-1}$, so that what is plotted is the energy emitted per accreted nucleon. We show cases with standard ϵ_ν^C (*dotted lines*) and with ϵ_ν^C suppressed (*solid lines*). For comparison, we also show the temperature profile (*top panel, grey lines*) obtained with the results of Haensel & Zdunik (2003).

3.2. Superburst Ignition

⁴ The focus of this paper is how the thermal profile, and in particular the ignition depth of ^{12}C , changes when the additional nuclear physics is added to the outer crust. An exploration of the reactions in the inner crust is left for future work.

As shown in Fig. 2, the heat deposited in the outer crust is roughly 4 times greater than that computed in an approach that neglects captures into excited states. This greater heat release in the outer crust raises the temperature (Fig. 5) in the region where ^{12}C would unstably ignite, and hence one signature of this enhanced heating is a reduction in the ignition column depth y_{ign} for superbursts. We calculate the column depth y_{ign} for unstable carbon ignition using the composition from steady-state rp-process burning and the superburst ashes as described in § 2.2.2. These ashes do contain ^{12}C at mass fraction $X(^{12}\text{C}) = 0.08$. After solving for the thermal profile (Fig. 6), as described in § 3.1, we locate the ignition column y_{ign} using the one-zone stability analysis described in Cumming & Bildsten (2001). This point is indicated on the plot. The ignition column for the four models, from shallowest to deepest, are $y_{\text{ign}}/10^{12} \text{ g cm}^{-2} = 3.7, 4.8, 4.9,$ and 6.3 . The corresponding recurrence times are $t_{\text{rec}} = y_{\text{ign}}/\dot{m} = 5.6, 7.2, 7.4,$ and 9.5 yr . The change in outer crust composition from a single mass $A = 56$ with only captures into ground state to a realistic mixture of rp-process and superburst ashes shortens the recurrence time by about 20%. The increase in temperature at $y \lesssim 10^{12} \text{ g cm}^{-2}$ is much less dramatic between the two crust models. This is due in part because both the steady-state rp-process and the superburst produce mass chains that are devoid of captures at low μ_e (cf. Fig. 4).

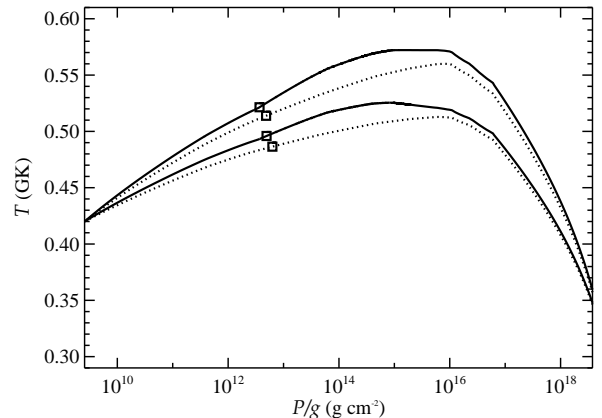


FIG. 6.— Thermal profiles for crusts with an outer layer of *steady-state* rp-process ashes, an outer crust composed of superburst ashes, with heating computed either by our network calculations (*solid lines*) or according to the model of Haensel & Zdunik (1990, *dotted lines*), and an inner crust computed from the model of Haensel & Zdunik (1990). The upper set of curves have the Cooper-pair neutrino emissivity suppressed.

We use the approximate model (§ 2.3) to investigate how the ignition depth depends on the heating in, and hence composition of, the outer crust. For each mass chain, we computed a thermal profile for a crust composed of that nuclide. As shown in Fig. 7, there is a wide variety in temperatures in the outer crust. The cases shown have the same boundary conditions as described in § 3.1, and the Cooper-pairing neutrino emission is suppressed according to Leinson & Perez (2006). As Fig. 4 shows there is a wide variation among the different A -chains in the amount of heat deposited and the deposition depth, which leads to a sizable difference in temperature at column $y \sim 10^{12} \text{ g cm}^{-2}$.

To follow how this variation in temperature affects the ignition depth, we then computed where a mixture of the crust material and ^{12}C , with $X(^{12}\text{C}) = 0.2$, would unstably ignite. The ignition points are shown in Fig. 7 (*black dots*),

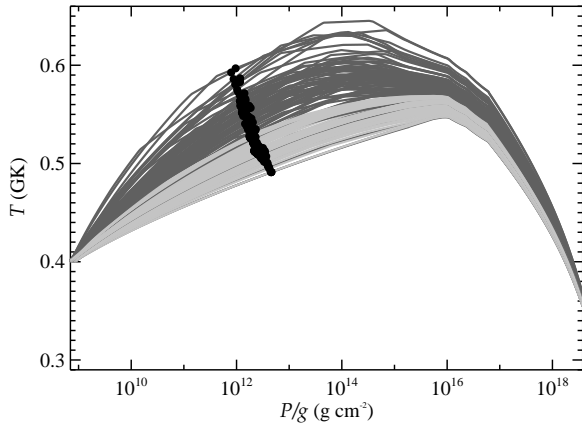


FIG. 7.— Temperature in the neutron star crust for mass chains with $A = 21$ –105. We show two models, one with captures into excited states included (*dark grey lines*) and one with only ground-state captures (*light grey lines*). In each case we set $\dot{M} = 3.0 \times 10^{17} \text{ g s}^{-1}$ and impose the same boundary conditions. Cooling by Cooper-pair neutrino emission is suppressed. For comparison, we also show for each model where ^{12}C would unstably ignite (*black dots*).

and we plot y_{ign} as a function of the mass chain A in Fig. 8 (*black histogram*). For comparison, we also show the ignition depth computed when captures into excited states are neglected (*grey histogram*). There is a general trend that the ignition depth decreases with increasing A , even for the case with no excitation energy. This is a consequence of two factors. First, the screening in a binary ionic mixture (Ogata, Ichimaru, & van Horn 1993) is enhanced by the presence of higher- Z nuclei. Second, the timescale for a temperature perturbation at a column of $10^{12} \text{ g cm}^{-2}$ to diffuse away increases by a factor ≈ 3 as A increases from 21 to 105. Both of these effects act to reduce the column needed to unstably ignite a ^{12}C -enriched plasma. This variation with A is probably exaggerated somewhat, because we did not self-consistently solve the thermal profile with the admixture of ^{12}C at $y < y_{\text{ign}}$, which would reduce the disparity in the mean value of Z and A among mass chains. Nevertheless, this exercise demonstrates how the superburst ignition depth depends on the makeup of the ashes of H and He burning, and the importance of correctly treating the underlying nuclear physics of the crust. The range of ignition columns is more consistent with the fitted recurrence times (Fig. 8, *thin dotted lines*) of Cumming et al. (2006, Table 1) when captures into excited states are included, but they are still not shallow enough to accommodate all of the inferred fits. To reduce further the ignition column would still require a reduction in the core neutrino emissivity below modified Urca, as suggested by Cumming et al. (2006).

If the Cooper-pairing neutrino emissivity is operating in the inner crust, then the ignition depth is further increased (Fig. 9). As before, however, the inclusion of electron captures into excited states reduces the discrepancy between the calculated y_{ign} and those fitted from observations.

4. SUMMARY AND CONCLUSIONS

We show that allowing for electron captures into excited states drastically increases the heat deposited into the outer crust of accreting neutron stars. The fraction of the reaction energy carried away by neutrinos is sharply curtailed. Neu-

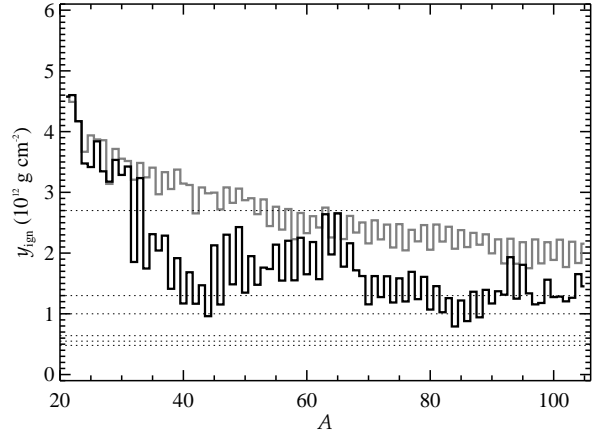


FIG. 8.— Carbon ignition depth y_{ign} for crusts composed of different mass chains A . The thermal profile is calculated using our approximate model with the Cooper-pairing neutrino emissivity suppressed. The difference in heating between the cases for which captures into excited states are included (*dark histogram*) and neglected (*grey histogram*) are clearly evident. For comparison, we also show the fitted ignition depths according to Cumming et al. (2006, Table 1) (*thin dotted lines*).

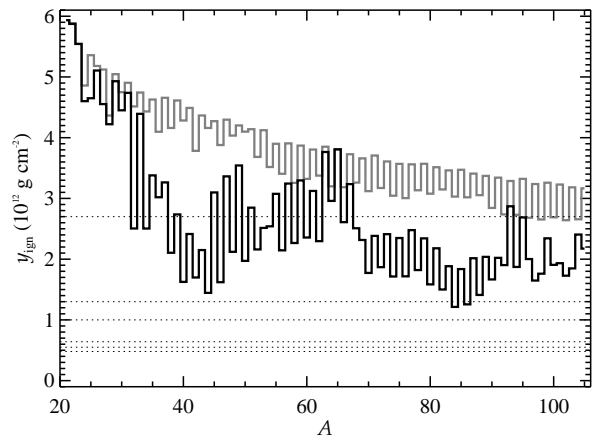


FIG. 9.— Same as Fig. 8, except that the Cooper-pairing neutrino emissivity is included.

trons released via (γ, n) reactions and recaptured by other nuclei provide an additional source of heating, and they can also serve as triggers for electron capture transitions as they shift matter to mass chains with different electron capture thresholds. We also find that the amount of heating in the crust is very sensitive to the initial composition forged during the burning of light elements in the neutron star envelope. This sensitivity is a consequence of the pronounced shell and sub-shell structure of neutron-rich nuclei, which can lead to drastic changes in shape, single particle level structure, and electron capture strength distributions, even between nuclei of similar Z, A .

We have explored how this increased deposition affects the ignition depth, and hence the recurrence time, of superbursts. For a realistic composition—steady-state rp-process ashes overlying superburst ashes—the inclusion of the excited states decreases the ignition depth by about 20%. For the most optimistic case we consider, in which the neutrino emissivity from Cooper-pairing is suppressed, the ignition depth for ac-

cretion at 0.3 Eddington is $y_{\text{ign}} = 3.7 \times 10^{12} \text{ g cm}^{-2}$, closer to the value inferred from observations ($y_{\text{ign}} = 5 \times 10^{11} - 2.7 \times 10^{12} \text{ g cm}^{-2}$; Cumming et al. 2006) although a significant discrepancy remains unless the core neutrino emissivity is reduced below the modified Urca rate.

To explore the variation of superburst ignition depths with composition, we have constructed an approximate model of the heating in the crust. Using this model, we find that at 0.3 Eddington, the superburst ignition depth can be as low as $8 \times 10^{11} \text{ g cm}^{-2}$ if the composition is dominated by nuclei with $A = 40-44$ or $A = 82-86$. The corresponding recurrence time for ignition at this depth, with the assumed accretion rate and neutron star parameters, is 1.2 yr. This is roughly in agreement with the observations, without invoking any additional physics. We are not aware, however, of a mechanism that would, for example, avoid the production of nuclei around $A \approx 60$ to dominate in superburst ashes.

Our results also indicate that crustal heating is very sensitive to the underlying nuclear physics. Reliable estimates of the structure of very neutron-rich nuclei up to $A = 106$ are needed to constrain the lowest lying electron capture strength, which determines the heating from the deexcitation of excited daughter states. Nuclear masses are needed to determine reac-

tion thresholds and neutron separation energies. And finally, masses, β^- decay rates, and reaction rates for the proton and helium induced reactions on very neutron deficient nuclei during hydrogen and helium burning in the αp - and rp -processes are needed to accurately determine the initial composition. More work is also needed to extend our calculations into the inner crust to determine the heating there.

It is a pleasure to thank Lars Bildsten, Andrew Cumming, and Dany Page for stimulating and fruitful conversations. We thank Friedel Thielemann for providing the network solver and Michelle Ouellette for contributing to the network code. This work is supported by the Joint Institute for Nuclear Astrophysics under NSF-PFC grant PHY 02-16783 and by NSF grant PHY 0110253. KLK acknowledges support from Virtuelles Institut für Struktur der Kerne und nukleare Astrophysik (VISTARS) under HGF grant VH-VI-061. This work was partially carried out under the auspices of the National Nuclear Security Administration of the U.S. Department of Energy at Los Alamos National Laboratory under Contract No. DE-AC52-06NA25396.

REFERENCES

- Ainsworth, T. L., Wambach, J., & Pines, D. 1989, *Phys. Lett. B*, 222, 173
 Akmal, A., Pandharipande, V. R., & Ravenhall, D. G. 1998, *Phys. Rev. C*, 58, 1804
 Becerril Reyes, A. D., Gupta, S., Kratz, K. L., Möller, P., & Schatz, H. 2006, *Proc. Sci.*, submitted
 Brown, E. F. 2000, *ApJ*, 531, 988
 Brown, E. F. 2004, *ApJ*, 614, L57
 Brown, E. F., Bildsten, L., & Chang, P. 2002, *ApJ*, 574, 920
 Cooper, R. L. & Narayan, R. 2005, *ApJ*, 629, 422
 Cumming, A. & Bildsten, L. 2001, *ApJ*, 559, L127
 Cumming, A. & Macbeth, J. 2004, *ApJ*, 603, L37
 Cumming, A., Macbeth, J., in 't Zand, J. J. M., & Page, D. 2006, *ApJ*, 646, 429
 Farouki, R. & Hamaguchi, S. 1993, *Phys. Rev. E*, 47, 4330
 Frevert, L., Schöneberg, R., & Flammersfeld, A. 1965, *Z. Phys.*, 185, 217
 Haensel, P. & Zdunik, J. L. 1990, *A&A*, 227, 431
 —. 2003, *A&A*, 404, L33
 in 't Zand, J. J. M., Cornelisse, R., & Cumming, A. 2004a, *A&A*, 426, 257
 in 't Zand, J. J. M., Cornelisse, R., Kuulkers, E., Verbunt, F., & Heise, J. 2004b, in *Proc. "X-Ray Timing 2003: Rossi and Beyond"*, ed. J. H. S. P. Kaaret, F. K. Lamb (Melville, NY: American Institute of Physics), in press (astro-ph/0407087)
 Itoh, N. & Kohyama, Y. 1993, *ApJ*, 404, 268
 Jones, P. B. 2004, *Phys. Rev. Lett.*, 93, 221101
 Kuulkers, E. 2003, in *The Restless High-Energy Universe*, ed. E. van den Heuvel, J. in 't Zand, & R. Wijers, *Nucl. Phys. B Suppl Series* (Elsevier)
 Kuulkers, E., in 't Zand, J., Homan, J., van Straaten, S., Altamirano, D., & van der Klis, M. 2004, in *X-ray Timing 2003: Rossi and Beyond*, ed. P. Kaaret, F. K. Lamb, & J. H. Swank (Melville, NY: AIP Press)
 Lattimer, J. M. & Prakash, M. 2001, *ApJ*, 550, 426
 Leinson, L. B. & Perez, A. 2006, *Phys. Lett. B*, 638, 114
 Mackie, F. D. & Baym, G. 1977, *Nucl. Phys. A*, 285, 332
 Möller, P., Nix, J. R., Myers, W. D., & Swiatecki, W. J. 1995, *At. Data Nucl. Data Tables*, 59, 185
 Möller, P. & Randrup, J. 1990, *Nucl. Phys. A*, 514, 1
 Negele, J. W. & Vautherin, D. 1973, *Nucl. Phys. A*, 207, 298
 Ogata, S., Ichimaru, S., & van Horn, H. M. 1993, *ApJ*, 417, 265
 Page, D. & Cumming, A. 2005, *ApJ*, 635, L157
 Pethick, C. J. & Ravenhall, D. G. 1998, in *Trends in nuclear physics*, 100 years later, ed. H. e. a. Nifenecker, *Les Houches Session LXVI*, 1996 (New York: Elsevier), 717
 Pethick, C. J. & Thorsson, V. 1994, *Phys. Rev. Lett.*, 72, 1964
 Rauscher, T. & Thielemann, F. 2000, *At. Data Nucl. Data Tables*, 75, 1
 Sato, K. 1979, *Prog. Theor. Physics*, 62, 957
 Schatz, H., Aprahamian, A., Barnard, V., Bildsten, L., Cumming, A., Ouellette, M., Rauscher, T., Thielemann, F.-K., & Wiescher, M. 2001, *Phys. Rev. Lett.*, 86, 3471
 Schatz, H., Bildsten, L., & Cumming, A. 2003, *ApJ*, 583, L87
 Schatz, H., Bildsten, L., Cumming, A., & Ouellette, M. 2003, *Nucl. Phys. A*, 718, 247
 Schatz, H., Bildsten, L., Cumming, A., & Wiescher, M. 1999, *ApJ*, 524, 1014
 Strohmayer, T. E. & Bildsten, L. 2004, in *Compact Stellar X-ray Sources*, ed. W. Lewin & M. van der Klis (Cambridge: Cambridge University Press), 113
 Strohmayer, T. E. & Brown, E. F. 2002, *ApJ*, 566, 1045
 Timmes, F. X. & Swesty, F. D. 2000, *ApJS*, 126, 501
 Tolman, R. C. 1939, *Physical Review*, 55, 364
 Wijnands, R. 2001, *ApJ*, 554, L59
 Yakovlev, D. G., Kaminker, A. D., & Levenfish, K. P. 1999, *A&A*, 343, 650